INTERNATIONAL JOURNAL FOR NUMERICAL METHODS IN ENGINEERING
Int. J. Numer. Meth. Engng 2006; **65**:1002–1027
Published online 7 September 2005 in Wiley InterScience (www.interscience.wiley.com). DOI: 10.1002/nme.1470

Stress integration and mesh refinement for large deformation in geomechanics

Majidreza Nazem[1], Daichao Sheng[1,*,†] and John P. Carter[2]

[1]*School of Engineering, The University of Newcastle, NSW, Australia*
[2]*Department of Civil Engineering, The University of Sydney, NSW, Australia*

SUMMARY

This paper first discusses alternative stress integration schemes in numerical solutions to large-deformation problems in hardening materials. Three common numerical methods, i.e. the total-Lagrangian (TL), the updated-Lagrangian (UL) and the arbitrary Lagrangian–Eulerian (ALE) methods, are discussed. The UL and the ALE methods are further complicated with three different stress integration schemes. The objectivity of these schemes is discussed. The ALE method presented in this paper is based on the operator-split technique where the analysis is carried out in two steps; an UL step followed by an Eulerian step. This paper also introduces a new method for mesh refinement in the ALE method. Using the known displacements at domain boundaries and material interfaces as prescribed displacements, the problem is re-analysed by assuming linear elasticity and the deformed mesh resulting from such an analysis is then used as the new mesh in the second step of the ALE method. It is shown that this repeated elastic analysis is actually more efficient than mesh generation and it can be used for general cases regardless of problem dimension and problem topology. The relative performance of the TL, UL and ALE methods is investigated through the analyses of some classic geotechnical problems. Copyright © 2005 John Wiley & Sons, Ltd.

KEY WORDS: large deformation; stress integration; arbitrary Lagrangian–Eulerian method; mesh motion

1. INTRODUCTION

Numerical solutions to large deformation problems have attracted the interest of many researchers during the last three decades. In the literature, there are different methods available for solving such problems of continuum mechanics by finite element analysis. These methods differ from each other mainly through the reference configurations used in the analysis. Bathe *et al.* [1] formulated two well-known methods namely the total-Lagrangian (TL) and the updated-Lagrangian (UL). In the TL method, the initial configuration of the body is used as the reference state and all variables (e.g. stresses and strains) are measured with respect

*Correspondence to: D. Sheng, School of Engineering, The University of Newcastle, NSW, Australia.
†E-mail: daichao.sheng@newcastle.edu.au

Received 23 May 2005
Revised 22 July 2005

to the initial configuration. In the UL method, the current configuration of the body is used during the analysis. It should be noted that the TL method and the UL method are not two different solutions to the problem, but rather two different ways of linearization of the equilibrium equations and should result in the same solution of the problem. In theory, they can both be used in problems with large deformations and large strains. The main drawback of the TL and UL methods is the loss of convergence and accuracy when severe mesh distortion occurs. Another approach, namely the arbitrary Lagrangian–Eulerian (ALE), has been developed more recently in an attempt to overcome the limitation of the TL and UL methods when severe mesh distortion occurs. In the ALE method, mesh distortion is avoided by re-meshing or mesh refinement, which is in turn accomplished by uncoupling the nodal displacements and the material displacements.

In this paper, we investigate alternative solution methods for large deformations and their relative performance in solving geotechnical problems. For continuity and completeness, we first present a brief description of the TL method and the UL method and different stress integration schemes used in these methods. An ALE method based on the split-operator technique is then presented, with a new scheme for mesh refinement. A number of classic geotechnical problems are then analysed to demonstrate the performance of these methods.

2. TOTAL-LAGRANGIAN AND UPDATED-LAGRANGIAN FORMULATION

2.1. Equilibrium equation

We assume that the analysis starts at time 0 and all state variables that satisfy equilibrium are known up to time t. Further loading and deformation of the body will require the equilibrium to be satisfied at time $t + \Delta t$. The principle of virtual work states that if δu is a virtual displacement field that satisfies the displacement boundary conditions, then equilibrium is satisfied provided

$$\int_{V^{t+\Delta t}} \sigma_{ij}^{t+\Delta t} \cdot \delta\varepsilon_{ij} \cdot \mathrm{d}V^{t+\Delta t} = R^{t+\Delta t} \tag{1}$$

where $\delta\varepsilon_{ij}$ is the variation of the strain tensor consistent with the virtual displacements δu, V is volume of the body, σ_{ij} is the Cauchy stress tensor, R denotes external work resulting from body forces and tractions, and the superscript denotes the time when the quantities are measured.

To solve Equation (1), all quantities must be transferred to a known configuration which can be either the initial configuration or the configuration at time t. In the so-called TL formulation, all variables are referred to the initial configuration at time 0. In the UL formulation, all variables are referred to the last equilibrium configuration at time t. The initial configuration of a point is usually specified by its initial co-ordinates X_i, and the current configuration can be represented by current co-ordinates x_i. These two system of co-ordinates are related to each other by displacement vector u_i, as following:

$$x_i = X_i + u_i \tag{2}$$

Equation (1) can now be transformed to the initial and current configuration, respectively, as

$$\int_{V^0} {}^0S_{ij}^{t+\Delta t} \cdot \delta {}^0E_{ij}^{t+\Delta t} \cdot \mathrm{d}V^0 = R^{t+\Delta t} \tag{3}$$

$$\int_{V^t} {}^tS_{ij}^{t+\Delta t} \cdot \delta {}^tE_{ij}^{t+\Delta t} \cdot \mathrm{d}V^t = R^{t+\Delta t} \tag{4}$$

where S_{ij} is the second Piola–Kirchhoff stress tensor, E_{ij} denotes the Green–Lagrange strain tensor, the right superscript denotes the time when the quantities are measured, and the left superscript denotes the configuration with respect to which the quantities are measured. The left subscript is dropped if the configuration with respect to which a quantity is measured is indicated elsewhere such as by V^0. The variables in Equation (3) are computed with respect to the initial configuration, while the variables in Equation (4) are computed with respect to the last equilibrium configuration at time t. The second Piola–Kirchhoff stress tensor is related to the Cauchy stress tensor through the deformation gradient F_{ij}

$$\sigma_{ij}^t = \frac{1}{J} F_{ik} S_{kl}^t F_{jl} \tag{5}$$

where J is the determinant of F which is defined by $F_{ij} = \partial x_i / \partial X_j$. The Green–Lagrange strain tensor is defined by

$$E_{ij} = \tfrac{1}{2} (u_{i,j} + u_{j,i} + u_{k,i}.u_{k,j}) \tag{6}$$

Linearization of Equations (3) and (4) eventually results in the following equations for the TL and UL methods, respectively,

$$\int_{V^0} \bar{C}_{ijkl}\, \mathrm{d}e_{kl} \delta(\mathrm{d}e_{ij})\, \mathrm{d}V^0 + \int_{V^0} S_{ij}^t \delta(\mathrm{d}\eta_{ij})\, \mathrm{d}V^0 = R^{t+\Delta t} - \int_{V^0} S_{ij}^t \delta(\mathrm{d}e_{ij})\, \mathrm{d}V^0 \tag{7}$$

$$\int_{V^t} \bar{C}_{ijkl}\, \mathrm{d}e_{kl} \delta(\mathrm{d}e_{ij})\, \mathrm{d}V^t + \int_{V^t} \sigma_{ij}^t \delta(\mathrm{d}\eta_{ij})\, \mathrm{d}V^t = R^{t+\Delta t} - \int_{V^t} \sigma_{ij}^t \delta(\mathrm{d}e_{ij})\, \mathrm{d}V^t \tag{8}$$

where $\bar{C}_{ijkl}$ is the stress–strain matrix derived from the constitutive relations $\mathrm{d}S_{ij} = \bar{C}_{ijkl} \cdot \mathrm{d}E_{kl}$, and $\delta(\mathrm{d}e_{ij})$ and $\delta(\mathrm{d}\eta_{ij})$ are the variations in the linear and non-linear parts of the incremental Green–Lagrange strain tensor, and for detailed expressions for them refer to Bathe [2].

In the linearization above, we used a stress–strain relation in terms of the second Piola–Kirchhoff stresses and the Green–Lagrange strain

$$\mathrm{d}S_{ij} = \bar{C}_{ijkl} \cdot \mathrm{d}E_{kl} \tag{9}$$

Instead of using a stress–strain relation like Equation (9), we often use the Cauchy stresses and the linear strains in constitutive laws. To do that, we have to introduce new, frame-independent

stress rates such as the Jaumann stress rate [3, 4]

$$\mathrm{d}\sigma_{ij}^{J} = \mathrm{d}\sigma_{ij} - \sigma_{ik}\,\mathrm{d}\Omega_{kj} - \sigma_{jk}\,\mathrm{d}\Omega_{ki} = C_{ijkl} \cdot \mathrm{d}\varepsilon_{kl} \tag{10}$$

where C_{ijkl} is the stress–strain matrix derived from the constitutive relations in terms of the Cauchy stresses and the linear strains, and Ω is the spin tensor given by

$$\Omega_{ij} = \frac{1}{2}\left(\frac{\partial u_i}{\partial x_j} - \frac{\partial u_j}{\partial x_i}\right) \tag{11}$$

Equation (10) implies that the total stress rate can be decomposed into a stress rate (Jaumann) due to straining and a stress rate due to rigid body motion. Introducing (10) into the virtual work equation, we can obtain the following equilibrium equation for the UL method based on the Jaumann stress rate:

$$\int_{V^t} C_{ijkl}\,\mathrm{d}\varepsilon_{kl}\delta(\mathrm{d}\varepsilon_{ij})\,\mathrm{d}V^t + \int_{V^t} (\sigma_{ik}^t\,\mathrm{d}\Omega_{jk} + \sigma_{jk}^t\,\mathrm{d}\Omega_{ik})\delta(\mathrm{d}\varepsilon_{ij})\,\mathrm{d}V^t + \int_{V^t} \sigma_{ij}^t\delta(\mathrm{d}\eta_{ij})\,\mathrm{d}V^t$$
$$= R^{t+\Delta t} - \int_{V^t} \sigma_{ij}^t\delta(\mathrm{d}\varepsilon_{ij})\,\mathrm{d}V^t \tag{12}$$

The first two terms on the left-hand side of Equation (12) are similar to those in Equation (8) and result in symmetric stiffness matrices, while the third term gives a non-symmetric contribution.

Another stress rate widely used in Geomechanics is due to Reference [5]

$$\sigma_{ij}^{t+\Delta t} = \sigma_{ij}^t + (C_{ijkl} + \Psi_{ijkl}) \cdot \mathrm{d}\varepsilon_{kl} \tag{13}$$

where Ψ_{ijkl} is used to account for the effects of rigid body motion. Substituting the relation

$$\mathrm{d}u_{i,\,j} = \mathrm{d}\varepsilon_{ij} + \mathrm{d}\Omega_{ij} \tag{14}$$

into the increment of Green–Lagrange strain tensor leads to

$$\mathrm{d}E_{ij} = \mathrm{d}\varepsilon_{ij} + \tfrac{1}{2}\,(\mathrm{d}\varepsilon_{ki} + \mathrm{d}\Omega_{ki})(\mathrm{d}\varepsilon_{kj} + \mathrm{d}\Omega_{kj}) \tag{15}$$

Taking the variation of the Green–Lagrange strain increment, $\delta(\mathrm{d}E_{ij})$, substituting it into Equation (4) and then eliminating the products of incremental quantities, leads to another UL formulation

$$\int_{V^t} \sigma_{ij}^t(\mathrm{d}\varepsilon_{ki}\delta(\mathrm{d}\varepsilon_{kj}) + \mathrm{d}\varepsilon_{ki}\delta(\mathrm{d}\Omega_{kj}) + \mathrm{d}\Omega_{ki}\delta(\mathrm{d}\varepsilon_{kj}) + \mathrm{d}\Omega_{ki}\delta(\mathrm{d}\Omega_{kj}))\,\mathrm{d}V^t$$
$$+ \int_{V^t} (C_{ijkl} + \Psi_{ijkl})\,\mathrm{d}\varepsilon_{kl}\delta(\mathrm{d}\varepsilon_{ij})\,\mathrm{d}V^t = R^{t+\Delta t} - \int_{V^t} \sigma_{ij}^t\delta(\mathrm{d}\varepsilon_{ij})\,\mathrm{d}V^t \tag{16}$$

The main advantage of using the Jaumann stress rate or the stress rate according to Chen and Mizuno [5] in the UL formulation is to simplify the stress integration scheme at Gauss points. In the following section, we will show that these stress rates enable us to extend the stress integration schemes used for small deformation to large deformation with relative ease.

2.2. Stress integration

For non-linear materials, the stress–strain relations are usually given in rate form and have to be solved by integration for a given strain increment. For small deformation, the stress integration is carried out in a form as

$$\begin{aligned} \sigma_{ij}^{t+\Delta t} &= \sigma_{ij}^{t} + \int_0^{\Delta\varepsilon_{kl}} C_{ijkl}(\sigma,\kappa)\cdot \mathrm{d}\varepsilon_{kl} \\ \kappa_i^{t+\Delta t} &= \kappa_i^{t} + \int_0^{\Delta\varepsilon_{kl}} B_i(\sigma,\kappa)\cdot \mathrm{d}\lambda = \kappa_i^{t} + \int_0^{\Delta\varepsilon_{kl}} B_i(\sigma,\kappa)\cdot D_{kl}(\sigma,\kappa)\cdot \mathrm{d}\varepsilon_{kl} \end{aligned} \tag{17}$$

where κ_i is a set of hardening parameters, C is the constitutive matrix depending on the current stresses and hardening parameters, B is a variable derived from the hardening laws and is typically a function of the current stresses and hardening parameters, $\mathrm{d}\lambda$ is the plastic multiplier that depends on the strain rate the current stresses and hardening parameters, and D is a vector derived from the consistency condition and the flow rule and is again a function of the current stresses and hardening parameters. An explicit stress integration scheme is differentiated from an implicit scheme by the stresses and hardening parameters used in evaluating C, B, and D.

For large deformation analysis, the stress–strain relations can no longer be expressed by Equation (17), due to possible rigid body motion. In the TL method, the stress and strain measures are, respectively, the second Piola–Kirchhoff stress tensor and Green–Lagrange strain tensor which are work-conjugate. An important property of these tensors is their invariability with respect to rigid body rotations and translations. In theory, the stresses and hardening parameters can be updated according to

$$\begin{aligned} {}^{0}S_{ij}^{t+\Delta t} &= {}^{0}S_{ij}^{t} + \int_0^{\Delta E_{kl}} C_{ijkl}({}^{0}S,\kappa)\cdot \mathrm{d}E_{kl} \\ \kappa_i^{t+\Delta t} &= \kappa_i^{t} + \int_0^{\Delta E_{kl}} B_i({}^{0}S,\kappa)\cdot \mathrm{d}\lambda = \kappa_i^{t} + \int_0^{\Delta E_{kl}} B_i({}^{0}S,\kappa)\cdot D_{kl}({}^{0}S,\kappa)\cdot \mathrm{d}E_{kl} \end{aligned} \tag{18}$$

Equation (18) is in the same form as (17), so that the stress integration scheme used for small deformation could be used here if C, B and D were known functions of S and κ. However, constitutive laws such as the yield functions and the hardening laws are rarely expressed in terms of the second Piola–Kirchhoff stresses and Green–Lagrange strains. Instead, they are usually defined in terms of the Cauchy stresses, and hence the constitutive matrix $C_{ijkl}(\sigma^t)$ is normally derived in terms of the Cauchy stresses

$$\dot{\sigma}_{ij} = C_{ijkl}\cdot \dot{\varepsilon}_{kl} \tag{19}$$

Using the relations between the two stress measures and the two strain measures, it is possible to derive the following relation from Equation (19)

$$\dot{S}_{ij} = (C_{mnst}\cdot J\cdot (F^{-1})_{im}\cdot (F^{-1})_{jn}\cdot (F^{-1})_{ks}\cdot (F^{-1})_{lt})\cdot \dot{E}_{kl} = \bar{C}_{ijkl}\cdot \dot{E}_{kl} \tag{20}$$

where F_{ij} is the deformation gradient from the current configuration to the initial configuration. Similarly, we can derive the incremental hardening laws between $\dot{\kappa}$ and $\dot{E}$:

$$\dot{\kappa}_i = \bar{B}_i\cdot \bar{D}_{kl}\cdot \dot{E}_{kl} \tag{21}$$

Note that the quantities $\bar{C}$, $\bar{B}$, and $\bar{D}$ are still functions of the Cauchy stresses. Therefore, the update scheme for the stresses and hardening parameters should be modified as

$$\begin{aligned} {}^0S_{ij}^t &\Rightarrow \sigma_{ij}^t \\ {}^0S_{ij}^{t+\Delta t} &= {}^0S_{ij}^t + \int_0^{\Delta E_{kl}} \bar{C}_{ijkl}(\sigma) \cdot \mathrm{d}E_{kl} \\ \kappa_i^{t+\Delta t} &= \kappa_i^t + \int_0^{\Delta E_{kl}} \bar{B}_i(\sigma, \kappa) \cdot \bar{D}_{kl}(\sigma, \kappa) \cdot \mathrm{d}E_{kl} \\ {}^0S_{ij}^{t+\Delta t} &\Rightarrow \sigma_{ij}^{t+\Delta t} \end{aligned} \tag{22}$$

If a substepping technique (such as in an explicit method) or an iteration technique (such as in an implicit method) is used, we have to transfer the second Piola–Kirchhoff stresses to the Cauchy stresses within each subincrement or each iteration. We also note that the yield function should always be checked with the Cauchy stresses during the stress integration. Stress integration schemes like (22) require significant changes over existing schemes for small deformation and may lead to divergence or instability due to the use of the two stress measures.

In the TL method by Bathe and Ozdemir [6], it is assumed that the Cauchy stresses in the constitutive laws can be directly replaced by the second Piola–Kirchhoff stresses so that the stress integration can be carried out as Equation (18). Such a scheme dramatically simplifies the integration, but will be shown to lead to inaccurate results in some cases.

In the UL method, the second Piola–Kirchhoff stresses at time $t + \Delta t$, but measured with respect to the configuration at time t , are first solved from the integration

$$\begin{aligned} {}^tS_{ij}^{t+\Delta t} &= {}^tS_{ij}^t + \int_0^{\Delta E_{kl}} \bar{C}_{ijkl}({}^tS) \cdot \mathrm{d}E_{kl} = \sigma_{ij}^t + \int_0^{\Delta E_{kl}} \bar{C}_{ijkl}({}^tS) \cdot \mathrm{d}E_{kl} \\ \kappa_i^{t+\Delta t} &= \kappa_i^t + \int_0^{\Delta E_{kl}} \bar{B}_i({}^tS, \kappa) \cdot \mathrm{d}\lambda = \kappa_i^t + \int_0^{\Delta E_{kl}} \bar{B}_i({}^tS, \kappa) \cdot \bar{D}_{kl}({}^tS, \kappa) \cdot \mathrm{d}E_{kl} \end{aligned} \tag{23}$$

where $C_{ijkl}({}^tS)$ is the constitutive matrix defined in terms of the current second Piola–Kirchhoff stresses measured with respect to the configuration at time t. Again, the derivation of such a constitutive matrix requires that all constitutive laws are given in terms of the second Piola–Kirchhoff stresses, which is seldom the case in reality. For the constitutive laws defined in terms of the Cauchy stresses, in principle, we need to transfer $\bar{C}$, $\bar{B}$, and $\bar{D}$ into C, B and D, according to Equation (20). However, we note that the deformation gradient is 1 at the start of the increment in the UL formulation and the quantities C, B and D are identical to $\bar{C}$, $\bar{B}$, and $\bar{D}$, respectively, when they are evaluated at the stress state σ^t. This means that, for an explicit integration scheme where these quantities are evaluated at the stress state σ^t, integration (23) can be carried out as

$$\begin{aligned} {}^tS_{ij}^{t+\Delta t} &= \sigma_{ij}^t + C_{ijkl}({}^t\sigma) \cdot \Delta E_{kl} \\ \kappa_i^{t+\Delta t} &= \kappa_i^t + B_i({}^t\sigma, \kappa) \cdot D_{kl}({}^t\sigma, \kappa) \cdot \Delta E_{kl} \end{aligned} \tag{24}$$

which is consistent with the corresponding explicit scheme for small deformation. In this case, the input is the Green–Lagrange strain increments, the current (Cauchy) stresses and the current hardening parameter, and the output is the second Piola–Kirchhoff stresses ${}^{t}S_{ij}^{t+\Delta t}$. Other quantities such as the gradients of the yield surface and plastic potential are evaluated exactly in the same way as for small deformation. Once ${}^{t}S_{ij}^{t+\Delta t}$ is known, the Cauchy (true) stresses are obtained by the transformation

$$\sigma_{ij}^{t+\Delta t} = \frac{1}{J} F_{ik} S_{kl}^{t+\Delta t} F_{jl} = \frac{1}{J} F_{ik} (S_{kl}^{t} + \Delta S_{kl}) F_{jl} = \frac{1}{J} F_{ik} (\sigma_{kl}^{t} + \Delta S_{kl}) F_{jl} \tag{25}$$

The above scheme can also be applied with a substepping technique, and the only requirement is that the Cauchy stresses must be obtained at the end of each subincrement.

Bathe *et al*. [1] initially used this integration scheme, but with the linear strain increment $\Delta\varepsilon$ instead of the Green–Lagrange strain increment ΔE. Later Bathe [2] used the Green–Lagrange strain increment ΔE in Equation (24). Rodriguez-Ferran *et al*. [7] and Rodriguez-Ferran and Huerta [8] showed that the scheme according to (24) and (25) is incrementally objective only if the Green–Lagrange strain increment is used in (24).

When the quantities $\bar{C}$, $\bar{B}$, and $\bar{D}$ are evaluated at a stress state $\sigma^{t+\alpha\Delta t}$ with $\alpha>0$, such as in an implicit scheme, the deformation gradient from the configuration at t to the configuration at $t+\alpha\Delta t$ is generally not 1 and hence $\bar{C}$, $\bar{B}$, and $\bar{D}$ are not identical to C, B and D. Therefore, the stress integration according to (24) and (25) is not applicable. However, we note that the second Piola–Kirchhoff stresses are actually not needed for solving the equilibrium equation for the UL method, i.e. Equation (8). Therefore, we can try to find the Cauchy stresses directly. Supposing ${}^{t}S_{ij}^{t+\Delta t}$ is known, the Cauchy stresses can be obtained by the transformation

$$\sigma_{ij}^{t+\Delta t} = \frac{1}{J} F_{ik} S_{kl}^{t+\Delta t} F_{jl} = \frac{1}{J} F_{ik} (\sigma_{kl}^{t} + \Delta S_{kl}) F_{jl} = \frac{1}{J} F_{ik} (\sigma_{kl}^{t}) F_{jl} + \Delta\sigma_{ij} \tag{26}$$

where the Cauchy stress increments can be estimated according to

$$\Delta\sigma_{ij} = \int_{0}^{\Delta\varepsilon_{kl}} C_{ijkl}(\sigma) \cdot \mathrm{d}\varepsilon_{kl} \tag{27}$$

The hardening parameters are then updated according to

$$\kappa_i^{t+\Delta t} = \kappa_i^{t} + \int_{0}^{\Delta\varepsilon_{kl}} B_i(\sigma, \kappa) \cdot \mathrm{d}\lambda = \kappa_i^{t} + \int_{0}^{\Delta\varepsilon_{kl}} B_i(\sigma, \kappa) \cdot D_{kl}(\sigma, \kappa) \cdot \mathrm{d}\varepsilon_{kl}$$

The stress integration according to Equations (27) and (26) is basically the same as that according to Equations (24) and (25), but is not limited to an explicit method. Gadala and Wang [9] used this scheme and showed that it is equivalent to the use of the Truesdell stress rate. In the remainder of this paper, the stress integration scheme according to Equations (24)–(25) or (27)–(26) is referred to as Bathe [2].

In the UL formulation using the Jaumann stress rate, the stress increment is found by integrating $\mathrm{d}\sigma_{ij}$ in Equation (10) along a given strain increment

$$\sigma_{ij}^{t+\Delta t} = \sigma_{ij}^{t} + \int_{0}^{\Delta\varepsilon_{ij}} \mathrm{d}\sigma_{ij} = \sigma_{ij}^{t} + \int_{0}^{\Delta\varepsilon_{kl}} C_{ijkl}(\sigma) \cdot \mathrm{d}\varepsilon_{kl} + \int_{0}^{\Delta\Omega_{kl}} (\sigma_{ik}\,\mathrm{d}\Omega_{jk} + \sigma_{jl}\,\mathrm{d}\Omega_{il}) \tag{28}$$

where $C_{ijkl}(\sigma)$ refers to the constitutive matrix with respect to the configuration at time t and is a function of the current Cauchy stresses. In this case, we no longer require that the constitutive laws be expressed in terms of the second Piola–Kirchhoff stresses. However, a stress integration scheme used for small deformation has to be modified to include the additional terms due to rigid body motion. Considering the skew-symmetry of $\Delta\Omega_{ij}$, it is possible to show that the second integration in (28) is equivalent to a stress transformation:

$$\sigma_{ij}^t + \int_0^{\Delta\Omega_{kl}} (\sigma_{ik}\,\mathrm{d}\Omega_{kj} + \sigma_{jl}\,\mathrm{d}\Omega_{li}) = Q_{ik}\sigma_{kl}^t Q_{jl} \tag{29}$$

with

$$Q_{ij} = (\delta_{ik} - \alpha\Delta\Omega_{ik})^{-1}(\delta_{kj} + (1-\alpha)\Delta\Omega_{kj})$$

where α is an integration parameter varying between 0 and 1. It is possible to show that the stress transformation (29) is objective if Q is orthogonal. Hughes and Winget [10] proved that the orthogonality of Q exists provided the strain increment and the spin tensor increment are evaluated with respect to the configuration at midpoint $t + \Delta t/2$ and $\alpha = 0.5$. Under these conditions, the stress integration can be carried out as

$$\begin{aligned} \bar{\sigma}_{ij}^t &= Q_{ik}\sigma_{kl}^t Q_{jl} \\ \sigma_{ij}^{t+\Delta t} &= \bar{\sigma}_{ij}^t + \int_0^{\Delta\varepsilon_{kl}} C_{ijkl}(\sigma)\cdot \mathrm{d}\varepsilon_{kl} \\ \kappa_i^{t+\Delta t} &= \kappa_i^t + \int_0^{\Delta\varepsilon_{kl}} B_i(\sigma,\kappa)\cdot D_{kl}(\sigma,\kappa)\cdot \mathrm{d}\varepsilon_{kl} \end{aligned} \tag{30}$$

The integration in (30) is almost identical to the integration in (17) for small deformation. The only modification is that the stresses at the start of the increment should be transformed according to $(30)_1$. Therefore, standard integration schemes used for small deformation, either explicit or implicit, can be used here to update the stresses and hardening parameters in (30).

In Chen and Mizuno's UL formulation, the stress–strain integration can be carried out in a similar way as for small deformation. The correction term due to rigid body motion is included in the matrix Ψ_{ijkl}, which is in turn added to the constitutive matrix. Again, both explicit and implicit schemes can be used here to update the stresses and hardening parameters

$$\sigma_{ij}^{t+\Delta t} = \sigma_{ij}^t + \int_0^{\Delta\varepsilon_{ij}} \mathrm{d}\sigma_{ij} = \sigma_{ij}^t + \int_0^{\Delta\varepsilon_{kl}} (C_{ijkl}(\sigma) + \Psi_{ijkl}(\sigma))\cdot \mathrm{d}\varepsilon_{kl} \tag{31}$$

Note that the objectivity of the integration according to (31) is not guaranteed.

To perform the stress-integration in each method discussed above, an explicit scheme is used based on the work by Sloan *et al*. [11]. This stress-integration scheme controls the error in the computed stresses by using a local error measure to automatically subincrement the applied strain increment. The error measure is computed at each integration point by taking the difference between a first-order accurate Euler solution and a second-order accurate modified Euler solution. The method has been used to solve problems involving a wide range of constitutive models for soils. The scheme that was originally used to perform stress integration defined

by Equation (17) is generalized here for large deformation, according to the modifications discussed above.

3. ARBITRARY LAGRANGIAN–EULERIAN FORMULATION

3.1. ALE preliminaries

In the TL and the UL methods, the mesh is adhered to the material so that both the mesh points and the material points move together during analysis. These two methods are suitable for problems where the domains do not suffer significant distortions. If the deformations are large, mesh distortion will be an obvious drawback to these two methods, as it tends to cause divergence and inaccuracy in the analysis. A possible solution to this problem is to re-mesh the distorted domain, which needs a remap of state variables from the distorted mesh to the new mesh. Remapping of state variables usually introduces additional inaccuracy and therefore the methods become impractical in problems where a large number of remeshing is necessary [12].

The basic idea of the ALE method is to separate the material and mesh displacements, which eliminates mesh distortion and entanglement of elements. In the ALE method the mesh is not connected to the material and indeed it can be arbitrary. Therefore, both the motion of the mesh and the material must be defined. Remapping of state variables is performed with the basic ALE kinematic formula [13]

$$\underline{\dot{f}} = \dot{f} + (v_i - v_i^r)\frac{\partial f}{\partial x_i} \tag{32}$$

where f is an arbitrary function, v_i is the material velocity, v_i^r is the mesh velocity, $\dot{f}$ denotes the time derivative of f with respect to mesh (grid points) co-ordinates, and $\underline{\dot{f}}$ represents the time derivative of f with respect to material co-ordinates. The term $v_i - v_i^r$ is called the convective velocity.

The discretized governing equation in the ALE method can be written in a general form as follows [14]:

$$[K_{ij}^{\mathrm{m}}]\{\Delta U_j\} + [K_{ij}^{\mathrm{r}}]\{\Delta U_j^{\mathrm{r}}\} = \{R_i\} - \{F_i\} \tag{33}$$

in which $K^{\mathrm{m}} =$ stiffness matrix related to material displacement vector; $K^{\mathrm{r}} =$ stiffness matrix related to mesh displacement vector; $U =$ material displacement vector; $U^{\mathrm{r}} =$ mesh displacement vector; $R =$ external load vector; and $F =$ internal force vector. Equation (33) shows that the material displacements and the mesh displacements are two unknowns at each degree of freedom. In other words, mesh displacements are coupled with material displacements and as a result the number of equations to be solved is doubled. In this case, supplementary equations are required to solve the equilibrium equation.

Another strategy called the ALE operator-split technique has been developed to decouple mesh displacements and material displacements in the coupled ALE method [15]. To solve the equilibrium equations by this technique, two steps are considered in the analysis: an UL step followed by an Eulerian step. In the UL step, the convection terms are neglected and the

UL method is used to solve the equilibrium equation. At the end of the UL step, the mesh may be distorted since it moves along with the material. Therefore, in the Euler step, a new mesh is generated for the deformed domain, based on the initial topology but without element distortion. All kinematic and static variables are then transferred from the old mesh to the new mesh using the relation between the material derivative and the mesh derivation.

3.2. Mesh movement

Determining the mesh movement in the ALE operator split technique is of great importance due to the convection phase in the Eulerian step (Equation (32)). Computing the convective velocity requires knowledge of both the material displacements and the mesh displacements. The material displacements are obtained at the end of the UL step which normally results in a distorted mesh. A new mesh is then generated for the deformed domain from which the mesh displacements can be found. Since the mesh motion is arbitrary in the ALE, there are several possibilities to find an optimum mesh and therefore different methods can be found in the literature, see e.g. References [14–18]. The most common method to determine the mesh motion is to remesh the domain by a mesh generation algorithm. For unstructured and general meshes, the Laplacian method provides a general solution for the optimum mesh by solving the Laplace differential equation in terms of the grid velocities. However, the mesh generated by Laplace method is usually distorted near boundaries with high curvatures [19]. Another strategy to determine the mesh motion is to use a basic mesh generation algorithm such as the transfinite mapping or the isoparametric mapping method (e.g. Reference [20]). Such a method is relatively efficient since the new mesh is usually obtained by solving an explicit equation. However, the number of elements on two opposite sides of a rectangular boundary must be the same which makes the method less applicable to complex geometries. More advanced mesh generation techniques, like Delaunay triangulation (e.g. Reference [21]), might be used for mesh optimization of irregular domains. One general short-coming of the methods mentioned above is the significant additional computation effort involved with mesh generation, topology changes and connectivity changes.

A new method, which is very simple but effective, will be presented here to determine the mesh displacements based on analytical studies of some elasticity problems. The method has been implemented for two-dimensional plane strain problems and axi-symmetric problems. However, it can easily be generalized to three-dimensional problems as well.

As mentioned earlier, mesh displacements and material displacements are uncoupled in the operator-split ALE method. The material displacements are obtained from the UL step. To obtain the mesh displacements, we first re-discretize all boundaries, which include the boundaries of the domain, the material interfaces and the loading boundaries. This procedure is depicted in Figure 1. Supposing the nodes on the undeformed boundaries (Figure 1(a)) are distorted after the UL step as shown in Figure 1(b), these nodes are then relocated on the deformed boundaries as shown in Figure 1(c). It should be noted that the normal component of the convective velocity on a boundary is zero, but not necessarily the tangential component. Therefore, the tangential component of the convective velocity must be considered when redefining the positions of these nodes.

The relocation of the nodes on boundaries can be done as follows. Supposing there are n nodes on an arbitrary boundary with global co-ordinates x_i and y_i, the polynomial defining

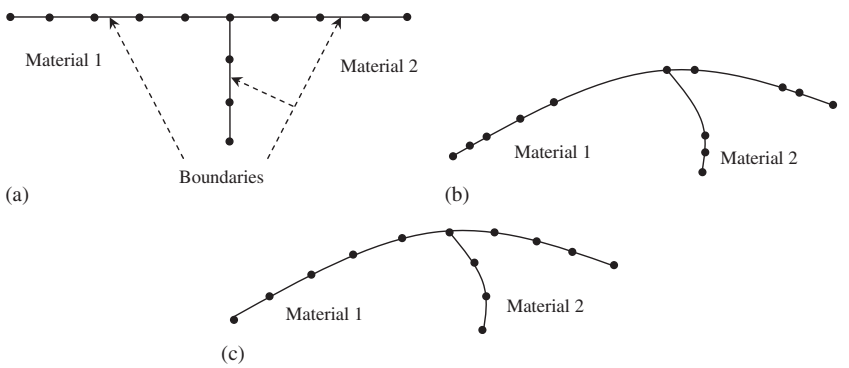

Figure 1. Relocation of nodes on the boundaries in two-dimensional cases: (a) boundaries before deformation; (b) boundaries at the end of UL step; and (c) boundaries after relocation of nodes.

this boundary, using quadratic spline technique [22], can then be written as

$$y = \begin{cases} \displaystyle\sum_{i=1}^{3} \left(y_i \cdot \prod_{\substack{j=1 \\ j\neq i}}^{3} \frac{(x - x_j)}{(x_i - x_j)} \right), & x_1 \leqslant x \leqslant x_3 \\ \displaystyle\sum_{i=3}^{5} \left(y_i \cdot \prod_{\substack{j=3 \\ j\neq i}}^{5} \frac{(x - x_j)}{(x_i - x_j)} \right) & x_3 \leqslant x \leqslant x_5 \\ \cdots\cdots\cdots\cdots\cdots\cdots\cdots\cdots & \\ \displaystyle\sum_{i=n-2}^{n} \left(y_i \cdot \prod_{\substack{j=n-2 \\ j\neq i}}^{n} \frac{(x - x_j)}{(x_i - x_j)} \right) & x_{n-2} \leqslant x \leqslant x_n \end{cases} \tag{34}$$

where

$$k = \frac{n-1}{2} \tag{35}$$

The length of the boundary, L, is then found by

$$L = \int_{x_1}^{x_n} \sqrt{1 + \left(\frac{\mathrm{d}y}{\mathrm{d}x} \right)^2}\, \mathrm{d}x \tag{36}$$

Knowing the length of the boundary, it is easy to redivide it to obtain a set of new nodes, redistributed spatially in some desired fashion.

With known displacements of these nodes on the boundaries, we then perform an elastic analysis using the mesh at time t and the prescribed displacements along the boundaries. This analysis assumes isotropic linear elasticity of a homogeneous medium and small deformation theory. Because we prescribe the displacements along all boundaries and material interfaces, the actual values of the elastic parameters used in this analysis are not important and one

set of elastic parameters can be used for the entire domain, regardless of the presence of real material interfaces. The incremental displacement components computed for each node from this elastic analysis are then added to the nodal co-ordinates of the mesh at time t to define the locations of the nodes in the new mesh at time $t + \Delta t$. The new mesh and the mesh at time t share the same connectivity. Such an elastic analysis should result in an optimal mesh if the nodes on the boundaries are optimally located. More importantly, such an analysis is very fast to complete, compared to the use of mesh generation processes, e.g. by triangulation.

Figure 2 represents a square continuum consisting of 256 triangular six-noded plain strain elements, with horizontal boundaries being rigid and rough and vertical boundaries being flexible and smooth. The material is represented by an associated Mohr–Coulomb model. A vertical compression leads to the deformed mesh in Figure 2(b). Two diagonal yield lines can be seen which are associated with severe distortion of the elements along the diagonals if the imposed strain is sufficiently large. To find a better mesh, the nodes on the deformed boundaries are first relocated using the technique described previously. The same problem is then re-solved using the original mesh and assuming a linear elastic medium, with the previously computed boundary displacements applied now as prescribed nodal displacements. The deformed mesh resulting from such an analysis is shown in Figure 2(c), where it is clear that this mesh does not show excessive distortion or element entanglement and can thus be used favourably in the ALE analysis of subsequent loading. The real advantage of this strategy is that mesh generation is required only for the domain and material boundaries. The method is mesh-independent and might be used for general two- or three-dimensional problems.

The mesh motion scheme proposed above can also be used for a coupled ALE method. In a coupled ALE method, the governing equations are written in terms of both material and mesh displacements and are supplemented by a set of equations relating the material displacements to the mesh displacements. A mesh motion scheme is used to solve the mesh displacements from the supplementary equations, once a trial set of the material displacements is known. The governing equations are then solved for the material displacements. The solution procedure is usually carried out in iterations. The proposed mesh motion scheme can be applied within each iteration to solve the supplementary equations.

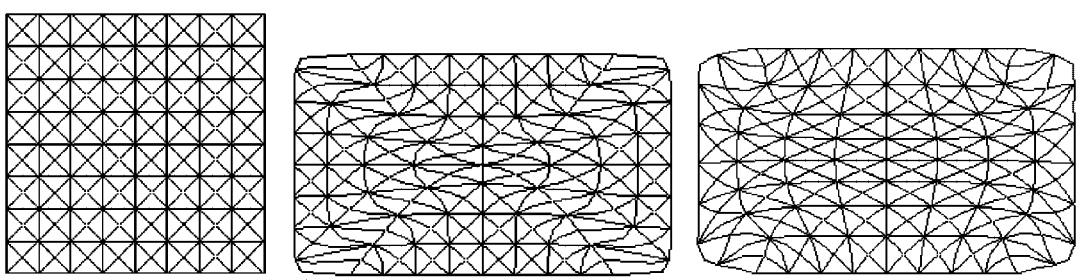

Figure 2. Demonstration of mesh refinement and mesh displacements: (a) initial mesh (545 nodes and 256 elements); (b) material displacements from elastoplastic analysis; and (c) refined mesh based on an elastic analysis with prescribed displacements.

3.3. Remapping state variables

Remapping of state variables from the old mesh to the new mesh during an ALE analysis is very important. The convection equation (32) involves the spatial derivatives of the function f. In the case of stresses, they may not be continuous across element boundaries and therefore their derivatives may not be computed reliably. To avoid computing the stress spatial derivatives, Liu *et al*. [16] introduced a stress–velocity product and computed its spatial derivatives instead. However, a weak form of stress integration had to be used. In this study, we will, however, use the common convection equation (32), but the nodal stresses being initially found from the integration points and then a continuous stress field is assumed in an element using its shape functions.

In the ALE method based on the operator-split technique, the numbers of elements and nodes are constant during the analysis and the nodal points are free to move arbitrarily. Therefore, this technique could be categorized as the r-adaptive finite element. In r-adaptive finite element, the state variables (e.g. stresses) can be remapped from the old mesh to the new mesh using knowledge of the convective velocity and Equation (32). This procedure is explained here for stresses only. However, it can be generalized to other state variables like the hardening parameters. Multiplying Equation (32) by the time increment and substituting the stress for function f leads to

$$\sigma_{ij}^{r} = \sigma_{ij} + (u_k^r - u_k) \cdot \frac{\partial \sigma_{ij}}{\partial x_k} \tag{37}$$

where σ_{ij}^{r} are the stress components at the Gauss points of the new mesh and σ_{ij} are the stresses at Gauss points of the old mesh. Note that, in a coupled ALE method, the mesh displacements are also solved simultaneously as the material displacement. As such, the second term on the right-hand side of Equation (37) can be directly added to the stress integration [20].

For two-dimensional isoparametric elements, the stress gradients in Equation (37) are given as

$$\frac{\partial \sigma_{ij}}{\partial x_1} = \frac{\partial \sigma_{ij}}{\partial \xi} \cdot \frac{\partial \xi}{\partial x_1} + \frac{\partial \sigma_{ij}}{\partial \eta} \cdot \frac{\partial \eta}{\partial x_1}, \quad \frac{\partial \sigma_{ij}}{\partial x_2} = \frac{\partial \sigma_{ij}}{\partial \xi} \cdot \frac{\partial \xi}{\partial x_2} + \frac{\partial \sigma_{ij}}{\partial \eta} \cdot \frac{\partial \eta}{\partial x_2} \tag{38}$$

The derivatives of the stresses with respect to the normal co-ordinates, ξ and η, can be computed using the nodal shape functions N_i,

$$\frac{\partial \sigma_{ij}}{\partial \xi} = \sum_{k=1}^{n} \frac{\partial N_k}{\partial \xi} \cdot \sigma_{ij}^{k}, \quad \frac{\partial \sigma_{ij}}{\partial \eta} = \sum_{k=1}^{n} \frac{\partial N_k}{\partial \eta} \cdot \sigma_{ij}^{k} \tag{39}$$

where n is the number of nodes per element and σ_{ij}^{k} are nodal stresses. To compute the nodal stresses, the super convergent patch recovery technique developed by Zienkiewicz and Zhu [23] is used. In this method, it is assumed that the stress values in a patch are computed using a polynomial of the same order as the basic shape functions. Thus, for two-dimensional quadratic elements, the stresses may be written as

$$\boldsymbol{\sigma} = \mathbf{P} \cdot \mathbf{a} \tag{40}$$

where the matrix notation is used instead of the component notation and

$$\mathbf{P} = [1, x, y, x^2, xy, y^2] \tag{41}$$

$$\mathbf{a} = [a_1, a_2, a_3, a_4, a_5, a_6]^{\mathrm{T}} \tag{42}$$

Zienkiewicz *et al*. [24] proposed the use of normalized co-ordinates in Equation (41) instead of global co-ordinates to avoid ill-conditioning of equations, particularly for higher order elements. The normalized co-ordinates in a two-dimensional patch, x_i^* and y_i^*, can be written as

$$x_i^* = -1 + 2\frac{x_i - x_{\min}}{x_{\max} - x_{\min}}, \quad y_i^* = -1 + 2\frac{y_i - y_{\min}}{y_{\max} - y_{\min}} \tag{43}$$

where $x_{\min}$ and $x_{\max}$ represent the maximum and minimum values of the x-co-ordinates in the patch, respectively, and $y_{\max}$ and $y_{\min}$ are defined similarly for the y-co-ordinates.

A least-square fit is then used to find the unknown values of $\mathbf{a}$ by minimizing

$$F(\mathbf{a}) = \sum_{i=1}^{m} (\sigma(x_i^*, y_i^*) - \mathbf{P}(x_i^*, y_i^*).\mathbf{a})^2 \tag{44}$$

in which $\sigma(x_i^*, y_i^*)$ are the stress values at Gauss points and m is the number of Gauss points in a patch. Finally, $\mathbf{a}$ is found by

$$\mathbf{a} = \mathbf{A}^{-1}\mathbf{b} \tag{45}$$

where

$$\mathbf{A} = \sum_{i=1}^{m} \mathbf{P}^{\mathbf{T}}(x_i^*, y_i^*)\mathbf{P}(x_i^*, y_i^*) \tag{46}$$

$$\mathbf{b} = \sum_{i=1}^{m} \mathbf{P}^{\mathbf{T}}(x_i^*, y_i^*)\sigma(x_i^*, y_i^*) \tag{47}$$

The stresses at any node in the patch can now be obtained by substituting its normalized co-ordinates in Equation (40).

For elastoplastic materials, the stresses and hardening parameters updated according to the above algorithm are not guaranteed to lie inside or on the yield surface, unless constant-stress triangular elements (with one integration point) are used. That again raises the issue of objectivity for the remapping of the stresses and hardening parameters. In theory, remapping of the state variables from an old mesh to a new mesh should not cause any straining and hence the equilibrium should be satisfied for both the old and new mesh. Unfortunately, there is no simple way to guarantee this objectivity. In this paper, if a stress point after remapping is found outside the yield surface, it is projected back to the yield surface according to the correction scheme for yield surface drift suggested by Sloan *et al*. [11].

An alternative remapping strategy is to remap the strains and to re-integrate stress–strain relations to find the stresses for the new mesh [25, 26]. During this procedure, the internal variables such as plastic strains are first projected from the Gauss points to the nodal points of

the old mesh using a least-square method and the element shape functions. The nodal internal variables as well as the displacement fields are then remapped to the new mesh. The internal variables and the strains at the Gauss points of the new mesh are obtained by interpolating the shape functions of the elements. The stresses at the integration points of the new mesh are then found by integrating the constitutive equations over the total strains. The stresses so found are guaranteed to be on the yield surfaces. However, the equilibrium of the system is not guaranteed, and hence the objectivity of the remapping procedure is not guaranteed. In addition, as the stress integration in the new mesh is not along a strain increment, but the total strain, it is difficult to apply this strategy to problems with an initial stress field or to constitutive models that depend on the stress path.

3.4. ALE algorithm

This section briefly summarizes the ALE algorithm used in this study. An incremental analysis is performed due to material and geometric non-linearities. Standard load-stepping techniques such as Newton–Raphson or Modified Newton–Raphson can be used. The procedure explained below is carried out during each load step.

Phase 1—UL step:

1. Assemble the global stiffness matrix and load vector and solve for incremental displacements, Δu.
2. Compute the strain increments and update the stresses and hardening parameters.
3. Iterate until the unbalanced forces are smaller than a prescribed tolerance.
4. Update the material co-ordinates: $\mathrm{COORDM} = \mathrm{COORDM} + \Delta u$.

Phase 2—Eulerian step:

1. Compute nodal stresses using the procedure described in Section 3.3.
2. Check the boundaries and relocate the nodes on the boundaries wherever necessary.
3. Compute the new mesh co-ordinates by performing an elastic analysis and store them in COORDG.
4. Remap state variables (stresses and hardening parameters) onto the new mesh co-ordinates using Equation (32).
5. Update the total displacements vector: $u = u + \mathrm{COORDG} - \mathrm{COORDM}$.
6. Set the material co-ordinates equal to mesh co-ordinates for next time step.
7. Compute internal forces, check equilibrium and conduct further iterations if necessary.

Ideally, the unbalanced forces at the end of Step 6 in Phase 2 should be small so that the equilibrium of the system is retained. Indeed, if the remapping of the stresses and hardening parameters is objective, equilibrium is mostly likely. As such, the equilibrium check in Step 7 gives a convenient indication of the objectivity of the stress remapping. However, since this objectivity is not guaranteed, additional iterations to reduce the unbalanced forces at the end of Step 6 may be required. Test runs for the problems analysed in this paper indicate that $2 \sim 4$ additional iterations are typically required after the mesh refinement and stress remapping. If such iterations indeed occur, the resulting displacements have to be added to the total nodal displacements, as a correction to the non-objective stress remapping.

4. NUMERICAL EXAMPLES

The algorithms for large deformations described above have been implemented in the finite element code, SNAC, developed at the University of Newcastle, Australia, over the last two decades. This code is used for all the numerical examples presented in this section. All the examples are analysed using six-noded isoparametric triangular elements, with six integration points. To avoid complications, we use the standard Newton–Raphson method to solve the non-linear global equilibrium equations, even though more advanced solution schemes for non-linear problems are available in the code SNAC [27, 28]. At the Gauss points, the stress integration is carried out using the explicit scheme suggested by Sloan *et al.* [11].

Although the methods described in this paper can be used to analyse general large deformation problems in continuum mechanics, we limit our applications here to geotechnical problems. Geotechnical problems involving large deformations have been addressed by many others, e.g. [4, 29–33]. Hu and Randolph [34] also applied an ALE method to solve the penetration of spudcan foundations. Penetration problems, including penetration of piles and testing devices into the ground, are extremely difficult to simulate, but the ALE methods should be well suited to their numerical solution. Such problems are not addressed in this paper because they also involve additional complexities such as contact mechanics and pore pressure dissipation.

4.1. Rigid strip footing

In the first example, we analyse a rigid smooth strip footing resting on an associated Mohr–Coulomb material. The right-hand half of the footing is shown in Figure 3. The material properties are also listed in Figure 3, where $E =$ Young's modulus; $\nu =$ Poisson's ratio; $c =$ cohesion; $\phi =$ friction angle, and $\psi =$ dilation angle.

The average vertical pressure under the footing is plotted against the applied vertical displacement in Figure 4. The small-deformation analysis results in a predicted collapse load of approximately 1.2 MPa mobilized at a prescribed settlement of approximately 3 cm. The UL methods with different implementations lead to almost identical results, without an obvious collapse load able to be identified from the load–displacement curve, at least for the range of footing displacements considered here. The load capacity at 3 cm settlement is about 1.27 MPa. The ALE method gives the same results as the three UL methods in this case, because over

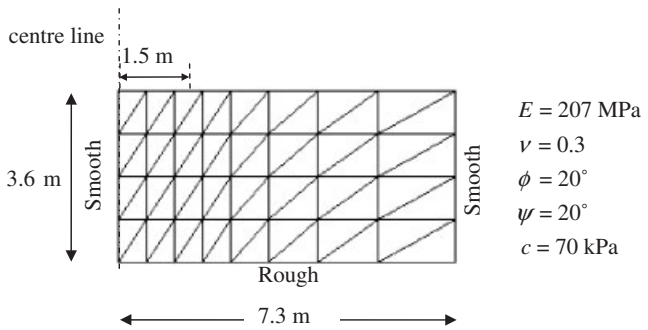

Figure 3. Rigid strip footing on Mohr–Coulomb soil ($B/2 = 1.5$ m, six-noded triangular elements).

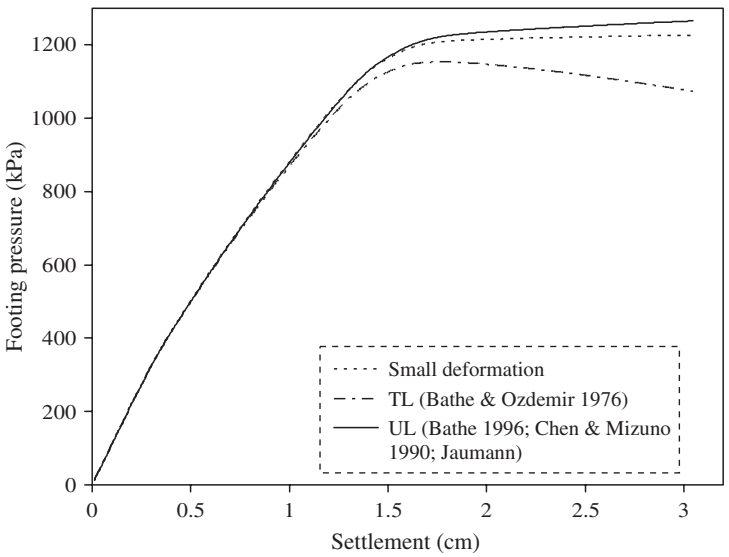

Figure 4. Load–displacement response of the rigid smooth footing on Mohr–Coulomb soil.

Table I. CPU time and total equilibrium iterations in each method.

Method	CPU time (s)	Total iterations
Small deformations	5	509
TL [6]	5	507
UL [2]	9	505
UL [5]	23	1660
UL (Jaumann)	8	507

this limited range of footing displacements mesh distortion is not significant. For clarity, the results of ALE method are not shown in Figure 4.

The load–displacement curve for the TL method is obtained by assuming that the second Piola–Kirchhoff stresses can replace the Cauchy stresses in the Mohr–Coulomb yield function. The stress integration can thus be carried out according to Equation (18). Bathe and Ozdemir [6] first used such an assumption in their TL formulation. The load–displacement curve in Figure 4 is descending after reaching a peak load, which is identical to the result obtained by the commercial finite element code ADINA. The results shown here indicate that replacing the Cauchy stresses in the constitutive laws by the second Piola–Kirchhoff stresses does not lead to the correct solution at large deformation. In fact, S_{ij} is only close to σ_{ij} for small deformation when the deformation gradient F_{ij} is close to unity.

In this example, all solution methods for large deformations furnish a solution and the results given by the UL and ALE methods are not much different from that given by the small-deformation analysis. Table I gives the CPU times and the number of equilibrium iterations for

each analysis. The two objective UL methods, i.e. based on Bathe [2] and on the Jaumann stress rate, are significantly faster than the non-objective UL method based on Reference [5]. This result indicates that the non-objectivity of the stress integration does lead to more equilibrium iterations, but does not significantly affect the accuracy, at least not in this case.

4.2. Rigid footing on undrained soil

In the second example, we consider a rigid rough footing on an undrained soil layer represented by the associated Tresca model. The mesh for the right-hand half of the footing and the material properties are shown in Figure 5. The mesh consists of 872 six-noded plane-strain triangular elements with 1817 nodes. The total imposed displacement is 2.5 times the half footing width B, compared to $0.02B$ used in the previous example. Due to this large settlement and the incompressibility of the soil ($v = 0.49$), we use a much finer mesh here than in Figure 2.

The predicted load–displacement curves are shown in Figure 6. The curve obtained by the small-deformation analysis shows a clear collapse load of $5.54c_u$, which is about 8% above the Prandl solution of plasticity theory, i.e. $(2 + \pi)c_u \approx 5.14c_u$. To obtain a more accurate collapse load, we would have to use a finer mesh and other types of elements like higher order elements.

The UL method based on Reference [5] is not able to finish the analysis up to the imposed displacement of $2.5B$, due to non-convergence in equilibrium iterations. The associated ALE method cannot complete the analysis either. The other two UL methods are able to complete the analysis. However, strong mesh distortion causes some oscillation in the load–displacement curve and no obvious collapse load is observed for these predictions. The ALE methods based on the Jaumann stress rate and Bathe [2] can also complete the analysis to the prescribed displacement and it is noticeable that their load–displacement curves are smoother than their UL counterparts. It also seems that the predictions of both ALE methods coincide with the exact collapse load

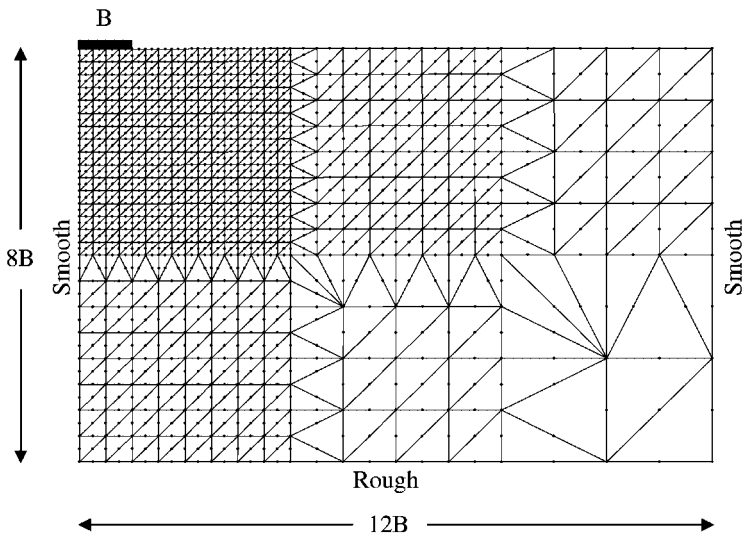

Figure 5. Rigid rough footing on cohesive soil ($B = 0.5$, $E/c_u = 100$, $v = 0.49$, $\phi = 0°$, $\psi = 0°$).

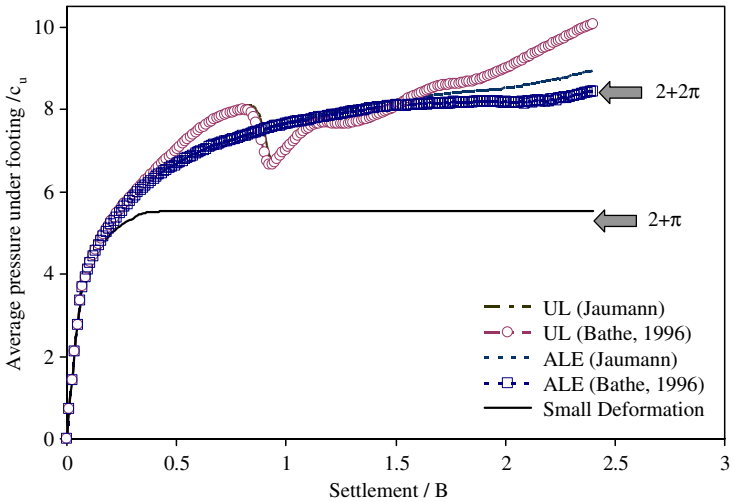

Figure 6. Load–displacement response of the rigid rough footing on undrained soil.

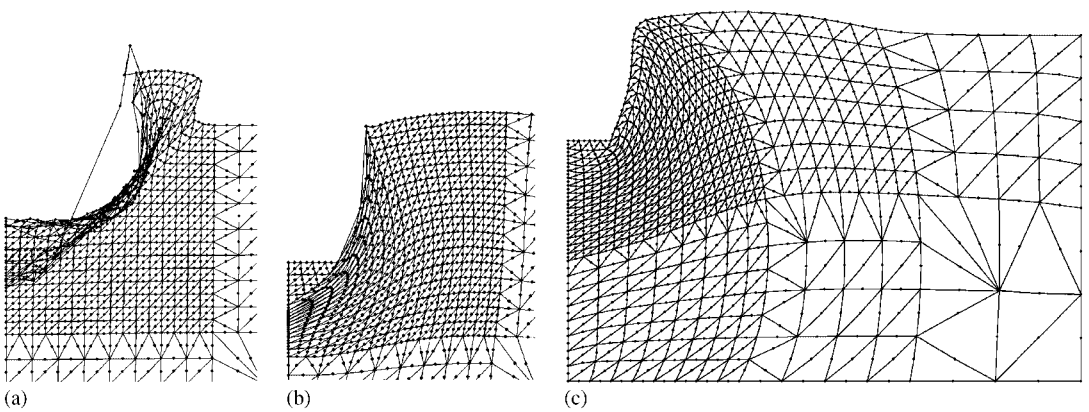

Figure 7. Deformed meshes for footing on undrained soil: (a) small deformation, settlement of $2.5B$; (b) UL (Jaumann), settlement of $2.5B$; and (c) ALE (Jaumann), settlement of $2.5B$.

for a rigid strip footing loaded at the bottom of a deep trench, i.e. $(2 + 2\pi)c_u \approx 8.28c_u$. Note that the latter is based on the small-deformation plasticity theory and the level of agreement between the two solutions may be somewhat fortuitous. In particular, the solution from plasticity theory corresponds to a trench with vertical sides, while this condition is not guaranteed *a priori* in the large displacement numerical solution.

The deformed meshes for this problem are shown in Figure 7. The deformed mesh for the small deformation analysis at a settlement of $2.5B$ is completely distorted (Figure 7(a)). In the small deformation analysis, the initial configuration was used at all stages of the analysis. The mesh plot shown in Figure 7(a) was produced simply by adding the final nodal displacements

to their corresponding nodal co-ordinates, to provide an overall impression of the effects of applying the footing load. The UL (Jaumann) deformed mesh at settlement of $2.5B$ is not very distorted in general, except that some elements start to have very high length–thickness aspect ratio (Figure 7(b)). Further loading will cause these elements to have negative Jacobian and hence the analysis to collapse. The ALE mesh at settlement of $2.5B$ remains in relatively good shape (Figure 7(c)).

Because the ALE method separates the material and mesh displacements, it is expected that its mesh refinement technique will smear, to some extent, stress concentration or strain localization, in particular when the refined elements are not sufficiently small to capture the areas of stress concentration or strain localization. In Figure 8, the stress distributions obtained by the ALE method are compared with those obtained by the UL method. It is clear that the ALE method does modify the stress fields locally, but gives overall stress distributions very close to those predicted by the UL method. It should be noted that the mesh distortion in the UL method at the settlement of $2.5B$ (Figure 7) is not very apparent. In order to study the true smearing effects of the ALE method, we may have to compare it with, for example, an h-adaptive finite element method. Nevertheless, one possible refinement to the ALE method is to consider the strain gradient when relocating the nodes on the boundaries.

Table II gives the CPU times and total equilibrium iterations for each method. For this example, the UL and ALE methods based on Jaumann stress rate clearly outperform their counterparts based on Bathe [2].

4.3. Rigid footing on soft clay modelled by the modified Cam clay model

In the third example, we test the algorithms for a more complex soil model that has commonly been used to model the behaviour of soft clays, i.e. the modified Cam clay (MCC) model. The MCC model is capable of modelling strain hardening and softening via one hardening parameter (the preconsolidation pressure, e.g. see References [35, 36]). Again, we investigate a rigid footing problem with the mesh shown in Figure 9.

Because the soil according to the MCC model has no strength at zero mean stress, we use the self weight of the soil to generate a non-zero initial stress field. In addition, we also add a thin layer of elastic material on top of the MCC soil to avoid a slope instability problem when the settlement of the footing is large, causing parts of the soil surface to become deeply inclined. The material properties used in the analysis are given in Figure 9, where λ is the slope of the normal compression line (NCL) in the space of the logarithmic mean stress $\ln p'$ versus the void ratio e, κ is the slope of the unloading–reloading line (URL) in the $\ln p - e$ space, e_{N} is the intercept of the NCL on the e axis when $\ln p' = 0$, OCR is the over-consolidation ratio of the soil, K_0 is the coefficient of earth pressure at rest, and γ is the unit weight of the soil. The parameters K_0 and γ are used to generate the initial stress field. The value of $K_0 = 1$ means the initial horizontal effective stress equals the initial vertical effective stress. The value of $\gamma = 6\ \mathrm{kN/m^3}$ corresponds to a bulk unit weight of $16\ \mathrm{kN/m^3}$ under submerged condition. Note that the yield surface of the MCC model used in the analysis is a rounded Mohr–Coulomb hexagon in the deviatoric plane [27].

The predicted load–displacement curves are shown in Figure 10 for the case of slowly applied loading allowing the soil to deform under fully drained conditions. The UL and ALE methods based on the Jaumann stress rate and Bathe [2] complete the analysis to the prescribed settlement of $3B$. The footing pressures predicted by the UL and ALE methods are not very

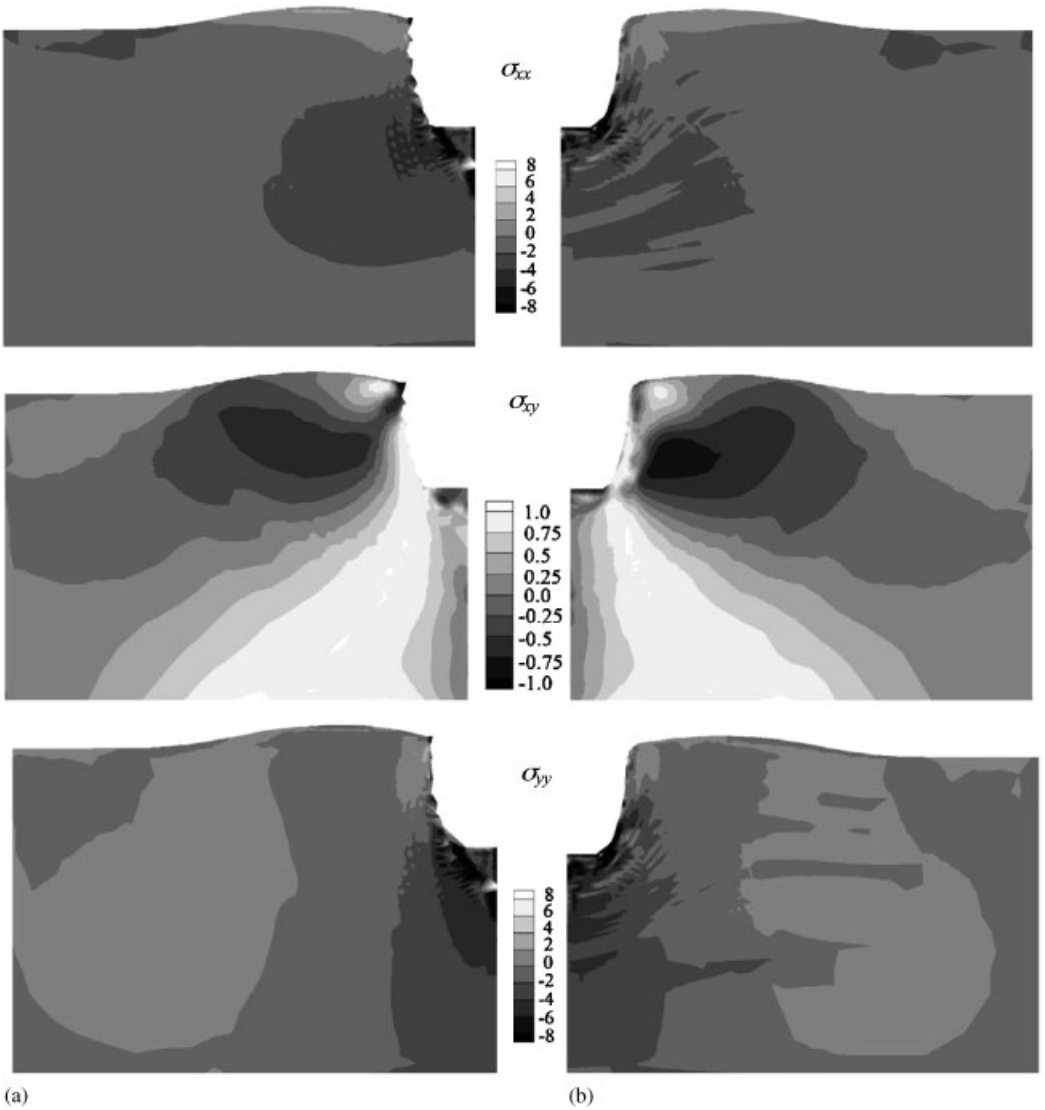

Figure 8. Stress distributions for the UL and ALE (Jaumann) analysis, settlement of $2.5B$: (a) UL; and (b) ALE.

different, but are significantly higher than the predictions of the small deformation analysis. The deformed meshes are shown in Figure 11. It is clear that when the displacements predicted by the small deformation analysis are added to their respective nodal co-ordinates, the resulting mesh is completely distorted. However, the mesh adopted in the UL method is not severely distorted and indeed and final UL mesh and the final ALE mesh are not significantly different, except for the locations of nodes along the interface between the top elastic layer and the MCC

Table II. CPU time and total equilibrium iterations in each method.

Method	CPU time (s)	Total iterations
Small deformations	318	283
UL [2]	1538	1426
UL (Jaumann)	1120	1053
ALE [2]	4268	3959
ALE (Jaumann)	3722	2008

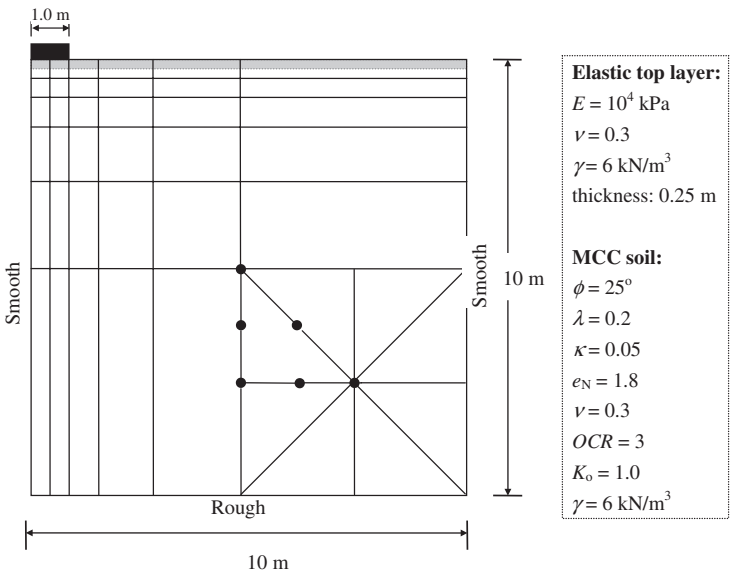

Figure 9. Finite element mesh (625 nodes and 288 elements) for the rigid footing on MCC soil.

soil. The UL and ALE methods based on Reference [5] again fail to converge to a solution for this example.

In the ALE analysis of this example, it is found that the remapping of the stresses and the hardening parameter according to Section 3.3 does not lead to the satisfaction of the yield criterion. The remapped stresses are then projected back to the yield surface according to the drift correction scheme suggested by Sloan *et al.* [11]. Furthermore, additional iterations, typically 3–4, are required to bring the new mesh to equilibrium.

Table III gives the performance data of the various methods in terms of CPU times and total equilibrium iterations. Again, the UL and ALE methods based on the Jaumann stress rate outperform their counterparts based on Bathe [6].

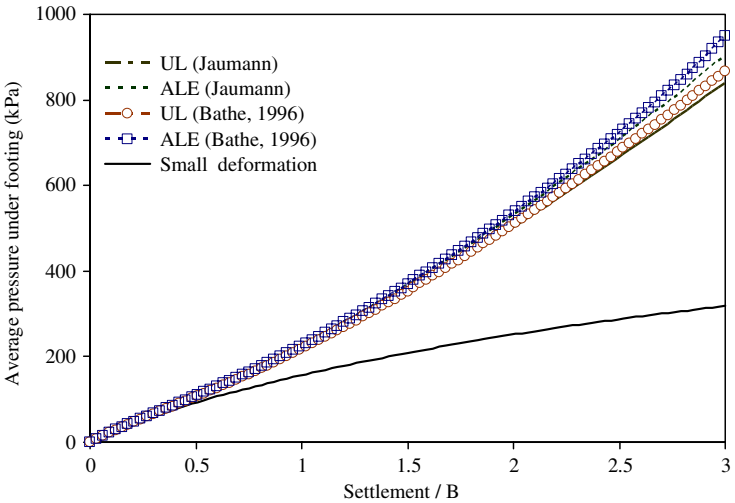

Figure 10. Load–displacement response of the rigid rough footing on the MCC soil.

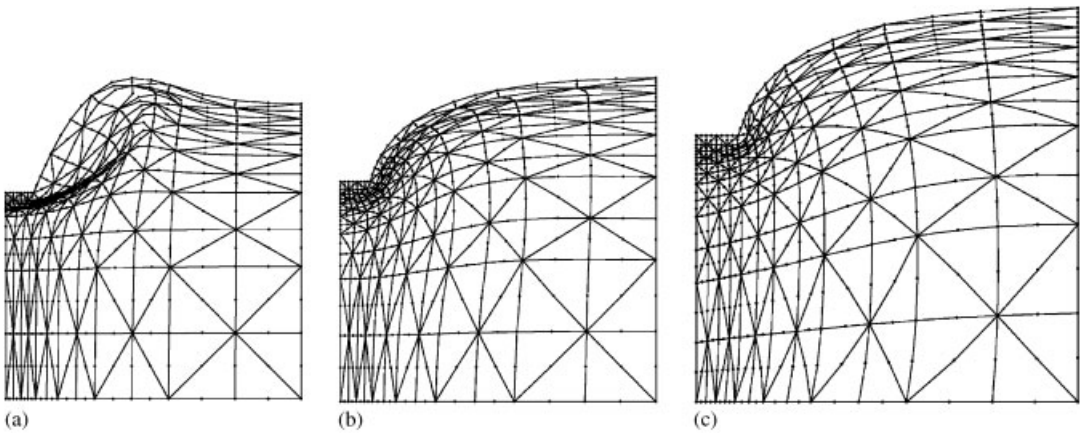

Figure 11. Deformed meshes for footing on MCC soil: (a) small deformation, settlement of $3B$; (b) UL (Jaumann), settlement of $3B$; and (c) ALE (Jaumann), settlement of $3B$.

5. CONCLUSIONS

This paper has discussed different stress integration schemes used in the numerical methods for large deformations and a new mesh refinement method for the ALE method. Some key conclusions drawn from this study are listed below.

1. The TL method is difficult to use in practice due to the difficulties in stress integration. Constitutive laws are usually defined in terms of the Cauchy stresses and the direct

Table III. CPU time and total equilibrium iterations in each method.

Method	CPU time (s)	Total iterations
Small deformations	102	322
UL [2]	258	771
UL (Jaumann)	216	542
ALE [2]	431	1361
ALE (Jaumann)	385	991

replacement of the Cauchy stresses by the second Piola–Kirchhoff stresses in the TL method can lead to inaccurate and incorrect results.

2. Three different formulations of the UL method are compared in this paper. These formulations include one based on the Truesdell stress rate or Bathe [6], Jaumann stress rate and the Chen and Mizuno [5] stress rate. The first two formulations incorporate objective stress integration schemes, while the objectivity of the stress integration scheme in the formulation by Chen and Mizuno [5] is not guaranteed. In terms of accuracy, the three schemes lead to more or less the same solution. However, in terms of robustness and efficiency, the UL method based on the Jaumann stress rate clearly outperforms the other two alternatives.
3. The ALE method based on the operator-split technique seems to provide an effective solution to the mesh distortion inherent in the UL method. The main challenges to the ALE method are the mesh refinement and the remapping of state variables.
4. The remapping of stresses and hardening parameters in the ALE method, based on convection, may not be objective, which implies that the remapped stresses and hardening parameters may violate the global equilibrium and the local consistency condition. There is no simple solution to this non-objectivity. In this paper, the consistency condition is enforced by projecting the stress states back to the yield surface according to a drift correction scheme which ensures that no strain is caused during the drift correction. Global equilibrium is achieved by additional Newton iterations after the remapping of stresses.
5. The proposed mesh refinement scheme works effectively and efficiently for the problems studied. An important advantage of this mesh optimization method is its independence of element topology and problem dimensions. The method does not require any mesh generation algorithm, does not change the global degrees of freedom or the connectivity of elements, and hence can be easily implemented in existing finite element codes. One possible improvement to the method is to consider the strain gradient when relocating the nodes along boundaries, i.e. the nodes can be more densely distributed where the strain gradient is highest.
6. Besides the examples presented in this paper, the ALE method should provide an ideal solution technique to geotechnical problems such as simulation of penetration of piles and testing devices into the ground. Such problems are extremely difficult to solve otherwise. They have been not addressed in this paper because they also involve other complexities like coupled pore pressure–displacement analysis and contact mechanics. Future work in this direction is deemed necessary.

REFERENCES

1. Bathe KJ, Ramm E, Wilson EL. Finite element formulations for large deformation dynamic analysis. *International Journal for Numerical Methods in Engineering* 1975; **9**:353–386.
2. Bathe KJ. *Finite Element Procedures*. Prentice-Hall: Englewood Cliffs, NJ, 1996.
3. Fung YC. *Foundations of Solid Mechanics*. Prentice-Hall: Englewood Cliffs, NJ, 1965.
4. Carter JP. Finite deformation theory and its application to elastoplastic soils. *Ph.D. Thesis*, University of Sydney, 1977.
5. Chen WF, Mizuno E. *Nonlinear Analysis in Soil Mechanics*. Elsevier: New York, 1990.
6. Bathe KJ, Ozdemir H. Elasto-plastic large deformation static and dynamic analysis. *Computers and Structures* 1976; **6**:81–92.
7. Rodriguez-Ferran A, Pegon P, Huerta A. Two stress update algorithms for large strains: accuracy analysis and numerical implementation. *International Journal for Numerical Methods in Engineering* 1997; **40**:4363–4404.
8. Rodriguez-Ferran A, Huerta A. Comparing two algorithms to add large strains to small-strain FE code. *Journal of Engineering Mechanics* 1998; **124**:939–948.
9. Gadala MS, Wang J. Computational implementation of stress integration in FE analysis of elasto-plastic large deformation problems. *Finite Elements in Analysis and Design* 2000; **35**:379–396.
10. Hughes TJR, Winget J. Finite rotation effects in numerical integration of rate constitutive equations arising in large-deformation analysis. *International Journal for Numerical Methods in Engineering* 1980; **15**:1862–1867.
11. Sloan SW, Abbo AJ, Sheng D. Refined explicit integration of elastoplastic models with automatic error control. *Engineering Computations* 2001; **18**:121–154.
12. Muttin F, Coupez T, Bellet M, Chenot JL. Lagrangian finite element analysis of time-dependent viscous free-surface flow using an automatic remeshing technique: application to metal casting flow. *International Journal for Numerical Methods in Engineering* 1993; **36**:2001–2015.
13. Hughes TJR, Liu WK, Zimmermann TK. Lagrangian–Eulerian finite element formulation for incompressible viscous flow. *Computer Methods in Applied Mechanics and Engineering* 1981; **58**:19–36.
14. Gadala MS, Wang J. ALE formulation and its application in solid mechanics. *Computer Methods in Applied Mechanics and Engineering* 1998; **167**:33–55.
15. Benson DJ. An efficient, accurate and simple ALE method for nonlinear finite element programs. *Computer Methods in Applied Mechanics and Engineering* 1989; **72**:305–350.
16. Liu WK, Belytschko T, Chang H. An arbitrary Lagrangian–Eulerian finite element method for path-dependant materials. *Computer Methods in Applied Mechanics and Engineering* 1986; **58**:227–245.
17. Liu WK, Chang H, Chen JS, Belytschko T. Arbitrary Lagrangian–Eulerian Petrov–Galerkin finite elements for nonlinear continua. *Computer Methods in Applied Mechanics and Engineering* 1988; **68**:259–310.
18. Gadala MS, Movahhedy MR, Wang J. On the mesh motion for ALE modeling of metal forming processes. *Finite Elements in Analysis and Design* 2002; **38**:435–459.
19. Belytschko T, Liu WK, Moran B. *Nonlinear Finite Elements for Continua and Structures*. Wiley: Chichester, NY, 2000.
20. Bayoumi HN, Gadala MS. A complete finite element treatment for the fully coupled implicit ALE formulation. *Computational Mechanics* 2004; **33**:435–452.
21. Sloan SW. A fast algorithm for generating constrained Delaunay triangulation. *Computers and Structures* 1993; **47**:441–450.
22. Lopez RJ. *Advanced Engineering Mathematics*. Addison Wesley: New York, 2001.
23. Zienkiewicz OC, Zhu JZ. The superconvergent patch recovery and a posteriori error estimates. Part 1: the recovery technique. *International Journal for Numerical Methods in Engineering* 1992; **33**:1331–1364.
24. Zienkiewicz OC, Zhu JZ, Wu J. Superconvergent patch techniques—some further tests. *Communications in Numerical Methods in Engineering* 1993; **9**:251–258.
25. Peric D, Hochard Ch, Dutko M, Owen DRJ. Transfer operators for solving meshes in small strain elasto-plasticity. *Computer Methods in Applied Mechanics and Engineering* 1996; **137**:331–344.
26. Peric D, Vaz Jr M, Owen DRJ. On adaptive strategies for large deformations of elasto-plastic solids at finite strains: computational issues and industrial applications. *Computer Methods in Applied Mechanics and Engineering* 1999; **176**:279–312.
27. Sheng D, Sloan SW. Load stepping methods for critical state models. *International Journal for Numerical Methods in Engineering* 2001; **50**(1):67–93.

28. Sheng D, Sloan SW. Time stepping schemes for coupled displacement and pore pressure analysis. *Computational Mechanics* 2003; **31**:122–134.
29. Carter JP, Booker JR, Davis EH. Finite deformation of an elasto-plastic soil. *International Journal for Numerical and Analytical Methods in Geomechanics* 1977; **1**:25–43.
30. Carter JP, Small JC, Booker JR. A theory of finite elastic consolidation. *International Journal of Solids and Structures* 1977; **13**:467–478.
31. Carter JP, Booker JR, Small JC. The analysis of finite elasto-plastic consolidation. *International Journal for Numerical and Analytical Methods in Geomechanics* 1979; **3**:107–129.
32. Wang C. Large deformation and no-tension analysis of selected problems in soil mechanics. *Ph.D. Thesis*, The University of Sydney, 2001.
33. Wang CX, Carter JP. Deep penetration of strip and circular footings into layered clays. *International Journal of Geomechanics* 2002; **2**(2):205–232.
34. Hu Y, Randolph MF. A practical numerical approach for large deformation problems in soils. *International Journal for Numerical and Analytical Methods in Geomechanics* 1998; **22**:327–350.
35. Muir Wood D. *Soil Behaviour and Critical State Soil Mechanics*. Cambridge University Press: Cambridge, MA, 1990.
36. Potts DM, Zdravkovic L. *Finite Element Analysis in Geotechnical Engineering*, vol. 1. Theory. Thomas Telford: London, 2001.

